



A Journal of



Accepted Article

Title: Rare-Earth Germanate Visible, Near-Infrared and Up-Conversion Emitters

Authors: Duarte Ananias, Filipe Almeida Paz, Luis D Carlos, and Joao Rocha

This manuscript has been accepted after peer review and appears as an Accepted Article online prior to editing, proofing, and formal publication of the final Version of Record (VoR). This work is currently citable by using the Digital Object Identifier (DOI) given below. The VoR will be published online in Early View as soon as possible and may be different to this Accepted Article as a result of editing. Readers should obtain the VoR from the journal website shown below when it is published to ensure accuracy of information. The authors are responsible for the content of this Accepted Article.

To be cited as: *Eur. J. Inorg. Chem.* 10.1002/ejic.201800153

Link to VoR: <http://dx.doi.org/10.1002/ejic.201800153>

WILEY-VCH

Rare-Earth Germanate Visible, Near-Infrared and Up-Conversion Emitters

Duarte Ananias,*^[a] Filipe A. Almeida Paz,^[a] Luís D. Carlos^[b] and João Rocha*^[a]

Abstract: The hydrothermal synthesis and structural characterization of new trivalent rare-earth germanates, $\text{Na}_4[(\text{Y}_{1-a}\text{Ln}_a)_2\text{Ge}_4\text{O}_{13}]$ ($\text{Ln} = \text{Eu}, \text{Tb}$ or Yb and Er ; $a = 0.05, 0.1$), and $\text{Na}_4[(\text{Yb}_{0.9}\text{Er}_{0.1})_2\text{Ge}_4\text{O}_{13}]$, are reported. The structure of these solids was solved by single-crystal X-ray diffraction (150 K). The materials crystallize in the orthorhombic non-centrosymmetric $Pna2_1$ space group, and exhibit a framework comprising unprecedented anionic tetrameric $[\text{Ge}_4\text{O}_{13}]^{10-}$ units, tetrameric units of $\{\text{GeO}_4\}$ tetrahedra, and isolated dimeric units encompassing two distinct distorted $\{\text{REO}_6\}$ octahedra. These rare-earth germanates feature interesting photoluminescence properties in the visible and near-infrared spectral regions. Eu^{3+} photoluminescence confirms the presence of two distinct rare-earth sites. Energy transfer between the latter sites is shown for $\text{Yb}^{3+}/\text{Er}^{3+}$ pair, both displaying a significant near-infrared emission. Isomorphous $\text{Na}_4[(\text{Yb}_{0.9}\text{Er}_{0.1})_2\text{Ge}_4\text{O}_{13}]$ features up-conversion emission, a unusual property among rare-earth crystalline germanates.

Introduction

In the past two decades we have been particularly interested on the synthesis and characterization of the luminescence properties of microporous, layered, and dense rare-earth (RE) silicates bearing optically-active trivalent lanthanide ions (Ln^{3+}).^[1-3] Some of these materials display unique and unusual photoluminescence. A case in point is the first example of a ratiometric cryogenic thermometer based on a dense Ln^{3+} silicate ($\text{Ln}=\text{Gd}, \text{Tb}, \text{Eu}$) whose emission properties depend on structural disorder and a phase transition.^[3c] Another example is microporous $\text{K}_7[\text{Eu}_3\text{Si}_{12}\text{O}_{32}]\cdot x\text{H}_2\text{O}$, an extended solid hosting framework $\text{Ln}^{3+}\text{-O-Ln}^{3+}$ dimers that behave like a molecule, as far as PL is concerned.^[1a] Yet another example is microporous chiral $\text{Na}_3[(\text{Y},\text{Ln})\text{Si}_3\text{O}_9]\cdot 3\text{H}_2\text{O}$ for which Eu^{3+} luminescence spectroscopy, with excitation by unpolarized light in the absence of an external magnetic field, is able to identify enantiomeric domains at 12 K.^[1b] Such enantiomeric detection was also achieved with partial substitution of Si^{4+} ions (up to 2/3) by Ge^{4+}

in the same material.^[4]

In contrast with RE silicates, luminescence accounts on RE germanates are scarce. In 2008 Chen *et al.*, studied the Eu^{3+} room-temperature luminescence of KEuGe_2O_6 , a cyclogermanate exhibiting zigzag chains of edge-sharing $\{\text{EuO}_6\}$ octahedra.^[5] Xu and collaborators, in 2012, studied the effect of pressure on the luminescence properties of both, NaEuGeO_4 ^[6] a material bearing $\{\text{EuO}_6\}$ octahedra linear chains and isolated $\{\text{GeO}_4\}$ tetrahedra, and of $\text{NaEu}_3(\text{GeO}_4)_2(\text{OH})_2$,^[7] featuring six-membered ring channels of $\{\text{EuO}_6\}$ octahedra. Luminescence of NaLnGeO_4 ($\text{Ln} = \text{Sm}, \text{Eu}, \text{Gd}, \text{Tb}$) has been further investigated by Yeon *et al.*^[8] The tunable emission capability of $\text{K}_3[\text{Tb}_x\text{Eu}_{1-x}\text{Ge}_3\text{O}_8(\text{OH})_2]$ ($x = 1, 0.88, 0.67, 0$)^[9] and the Gd^{3+} -to- Tb^{3+} energy-transfer process in $\text{K}_3[\text{Gd}_{1-x}\text{Tb}_x\text{Ge}_3\text{O}_8(\text{OH})_2]$ ($x = 0, 0.3, 0.1, 1$),^[10] a family of layered compounds structurally analogous to $\text{K}_3\text{LnSi}_3\text{O}_8(\text{OH})_2$ ($\text{Ln} = \text{Y}^{3+}, \text{Eu}^{3+}, \text{Tb}^{3+}, \text{Er}^{3+}$),^[2a] have also been discussed.

Here, we wish to report the new RE germanate system, $\text{Na}_4[(\text{Y}_{1-a}\text{Ln}_a)_2\text{Ge}_4\text{O}_{13}]$ ($\text{Ln} = \text{Eu}, \text{Tb}$ or Yb and Er ; $a = 0.05, 0.1$), whose crystal structure consists of $\{\text{GeO}_4\}$ tetrahedra forming unprecedented tetrameric $[\text{Ge}_4\text{O}_{13}]^{10-}$ units, isolated dimeric units comprising two distinct distorted $\{\text{REO}_6\}$ octahedral, and charge-balancing Na^+ cations. These materials were prepared under mild hydrothermal conditions and present significant luminescence properties in the visible and near infrared spectral regions. Up-conversion emission was also demonstrated with the isomorphous compound $\text{Na}_4[(\text{Yb}_{0.9}\text{Er}_{0.1})_2\text{Ge}_4\text{O}_{13}]$.

Crystal Structure Description

$\text{Na}_4[(\text{Y}_{0.95}\text{Eu}_{0.05})_2\text{Ge}_4\text{O}_{13}]$ (**1**) was isolated as single-crystals suitable for X-ray diffraction (Experimental Section), crystallizing in the orthorhombic non-centrosymmetric $Pna2_1$ space group (Table 1) with two crystallographically distinct RE centers in the asymmetric unit (Figure 1). An unrestrained refinement of the crystal structure for the rates of occupancy of the mixed Y^{3+} and Eu^{3+} sites yielded ratios of 95% and 5%, similar to the synthesis gel and, thus, they were kept in the final structural model (and empirical formula). A search in the Inorganic Chemistry Database shows **1** is isotypical with a scandium-based material reported in the 1970s' by Gorbunov *et al.*^[11]

The two RE^{3+} centers coordinate to six $\{\text{GeO}_4\}$ tetrahedra in a typical distorted octahedral geometry, $\{\text{REO}_6\}$, with the two adjacent sites sharing an octahedral edge (Figure 1), forming a dimeric unit with a 3.5716(5) Å intermetallic $\text{RE}\cdots\text{RE}$ distance. Consider Table S1 in the supporting Information (SI). The two $\{\text{REO}_6\}$ coordination polyhedra have very similar $\text{RE-O}_{\text{average}}$ distances and $\Delta_{\text{max}}(\text{RE-O})$ maximum values: while for RE1 the RE-O distances range from 2.174(4) to 2.339(4) Å ($\Delta=0.165$ Å), for RE2 they are in the range 2.175(4)-2.329(4) Å ($\Delta=0.154$ Å).

[a] D. Ananias, J. Rocha, F. A. A. Paz
Department of Chemistry
CICECO – Aveiro Institute of Materials, University of Aveiro, 3810-193 Aveiro, Portugal
E-mail: dananias@ua.pt
rocha@ua.pt
Web page: www.ciceco.ua.pt

[b] L. D. Carlos
Department of Physics
CICECO – Aveiro Institute of Materials, University of Aveiro, 3810-193 Aveiro, Portugal

This similarity is also witnessed by the similar *cis* and *trans* O–RE–O bond angles (Table S2 in the SI).

Table 1. Crystal and structure refinement data of $\text{Na}_4[(\text{Y}_{0.95}\text{Eu}_{0.05})_2\text{Ge}_4\text{O}_{13}]$ (**1**).

Formula	$\text{Na}_4\text{Y}_{1.90}\text{Eu}_{0.10}\text{Ge}_4\text{O}_{13}$
Formula weight	3097.78
Crystal system	Orthorhombic
Space group	$Pna2_1$
$a/\text{\AA}$	14.7595(7)
$b/\text{\AA}$	5.5203(3)
$c/\text{\AA}$	15.4331(7)
Volume/ \AA^3	1257.44(11)
Z	1
$D_c/\text{g cm}^{-3}$	4.091
$\mu(\text{Mo-K}\alpha)/\text{mm}^{-1}$	18.805
Crystal size/mm	$0.06 \times 0.05 \times 0.05$
Crystal type	Colourless block
θ range	3.82 to 29.11
Index ranges	$-16 \leq h \leq 20$ $-7 \leq k \leq 7$ $-21 \leq l \leq 10$
Reflections collected	2767 [$R_{\text{int}} = 0.0234$]
Independent reflections	99.7%
Completeness to $\theta = 25.24^\circ$	$R1 = 0.0193$
Final R indices [$>2\sigma(I)$] ^[a,b]	$wR2 = 0.0446$ $R1 = 0.0205$
Final R indices (all data) ^[a,b]	$wR2 = 0.0450$ $m = 0.0287$
Weighting scheme ^[c]	$n = 1.7109$ 0.578 and $-0.737 \text{ e}\text{\AA}^{-3}$
Largest diff. peak and hole	

[a] $R1 = \sum ||F_o| - |F_c|| / \sum |F_o|$. [b] $wR2 = \sqrt{\sum [w(F_o^2 - F_c^2)^2] / \sum [w(F_o^2)^2]}$. [c] $w = 1 / [\sigma^2(F_o^2) + (mP) + nP]$ where $P = (F_o^2 + 2F_c^2)/3$

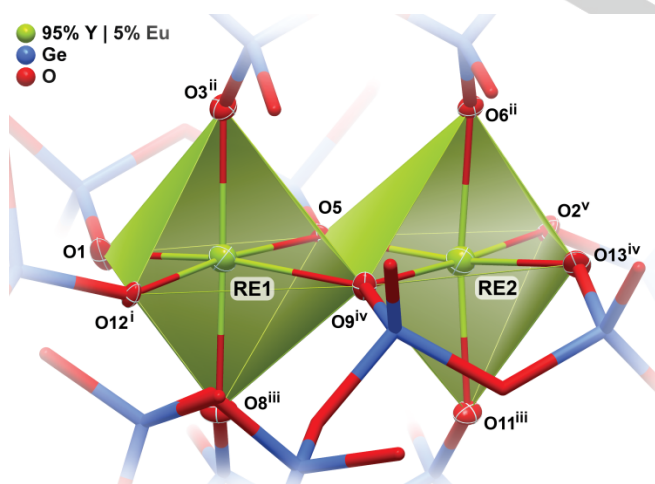


Figure 1. Schematic representation of the two distorted $\{\text{REO}_6\}$ octahedral coordination environments in $\text{Na}_4[(\text{Y}_{0.95}\text{Eu}_{0.05})_2\text{Ge}_4\text{O}_{13}]$ (**1**). Atoms forming the RE^{3+} coordination sphere are represented as thermal ellipsoids drawn at the 95% probability level. Selected bond lengths and angles are given in Tables S1 and S2, respectively. Symmetry transformations used to generate

equivalent atoms: (i) $-x+1/2, y-1/2, z+1/2$; (ii) $x, y-1, z$; (iii) $x-1/2, -y+1.5, z$; (iv) $x-1/2, -y+1/2, z$; (v) $-x+1/2, y-1/2, z-1/2$.

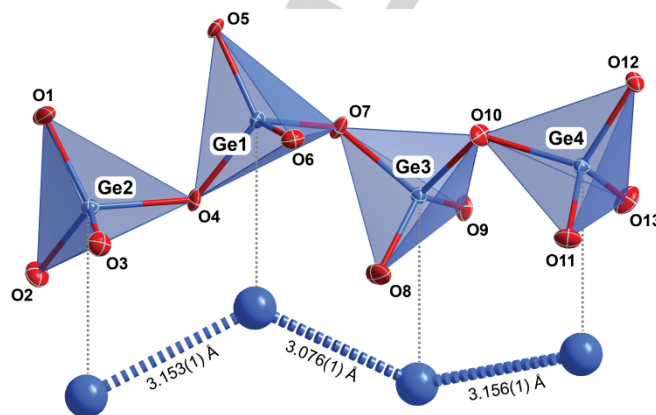


Figure 2. Tetrameric $[\text{Ge}_4\text{O}_{13}]^{10-}$ unit in $\text{Na}_4[(\text{Y}_{0.95}\text{Eu}_{0.05})_2\text{Ge}_4\text{O}_{13}]$ (**1**) viewed down the a -axis of the unit cell, depicting the individual $\text{Ge}\cdots\text{Ge}$ distances. Atoms are represented as thermal ellipsoids drawn at the 95% probability level. Selected bond lengths and angles are given in Tables 2 and 4, respectively.

The anionic unit comprises four crystallographically independent edge-shared $\{\text{GeO}_4\}^{4-}$ units with inter T-site distances ranging from 3.076(1) to 3.156(1) Å (Figure 2). Geometrical features of the central $\{\text{GeO}_4\}^{4-}$ units are slightly different from the periphery ones. First, for Ge1 and Ge3 the Ge–O distances are generally slightly longer and more regular than the distances observed for Ge2 and Ge4. This is witnessed by the calculated $\text{Ge-O}_{\text{average}}$ distances and $\Delta_{\text{max}}(\text{Ge-O})$ values given in Table S2 in the SI. Second, it is interesting to note that the less regular Ge2 and Ge4 tetrahedra also exhibit the smaller dispersion in internal O–Ge–O tetrahedral angles: while for Ge2 and Ge4 the tetrahedral angles are in the ranges $102.4(2)$ – $114.3(2)^\circ$ [$\Delta=11.9^\circ$] and $103.3(2)$ – $114.47(19)^\circ$ [$\Delta=11.2^\circ$], respectively, for Ge1 and Ge3 they span $101.0(2)$ – $120.39(19)^\circ$ [$\Delta=19.4^\circ$] and $101.5(2)$ – $122.1(2)^\circ$ [$\Delta=20.6^\circ$] (Table S4 in the SI). These structural variations are attributed to the steric pressure imposed on the two central $\{\text{GeO}_4\}^{4-}$ moieties by the tetrahedral corner sharing to form the tetrameric $[\text{Ge}_4\text{O}_{13}]^{10-}$ unit. Because of this, the two peripheral moieties are slightly more liberated to accommodate a more regular tetrahedral environment.

The anionic tetrameric $[\text{Ge}_4\text{O}_{13}]^{10-}$ unit interacts strongly with neighbouring RE^{3+} and Na^+ cations in the dense crystal structure of **1**. As shown in Figure S1 in the SI, each $\{\text{GeO}_4\}^{4-}$ moiety is connected to three RE^{3+} centers and, in general, to six Na^+ cations (except for Ge2, which only interacts with five Na^+). The closest $\text{Ge}\cdots\text{RE}$ distance is ca. 3.54 Å for Ge2, while the longest distance (ca. 3.74 Å) is observed for Ge3. Concerning the charge-balancing Na^+ cations, Ge4 exhibits the smallest $\text{Ge}\cdots\text{Na}$ dispersion (ca. 3.22–3.80 Å), with the opposite being observed for Ge2 (ca. 2.93–3.84 Å) (Figure S1 in the SI).

The crystal packing of **1** (Figure 3) may be rationalized by considering the close packing and mutual interactions between building units. The anionic tetrameric $[\text{Ge}_4\text{O}_{13}]^{10-}$ units occur in a typical herringbone fashion in the ac plane of the unit cell (Figure 3a), in what is one of the most efficient ways to head-to-tail close pack discrete linear units. $\{\text{Ge}_2\text{O}_{10}\}$ binuclear units, in turn, are also distributed in a herringbone fashion, and establish physical connections between adjacent tetrameric $[\text{Ge}_4\text{O}_{13}]^{10-}$ units (each dimer connecting to six symmetry-related anionic units), forming an anionic $[\text{RE}_2\text{Ge}_4\text{O}_{13}]_n^{4n-}$ network. This charged network has no solvent accessible volume (for a typical 1.2 Å probe radius),

as revealed by Mercury^[14] and PLATON.^[15] The available crystallographic voids are instead occupied by Na^+ cations (Figure 3c).

To reduce the anionic $[\text{RE}_2\text{Ge}_4\text{O}_{13}]_n^{4n-}$ network to nodes and connecting rods based on the structural features previously described, both the tetrameric $[\text{Ge}_4\text{O}_{13}]^{10-}$ unit and the RE dimer are considered nodes. Using the software package TOPOS,^[16] it is possible to infer that both nodes are six-connected and equivalent topologically, with the uninodal network exhibiting the **pcu** α -Po primitive cubic topological type. The framework topological description is depicted in Figures 3d and 3e.

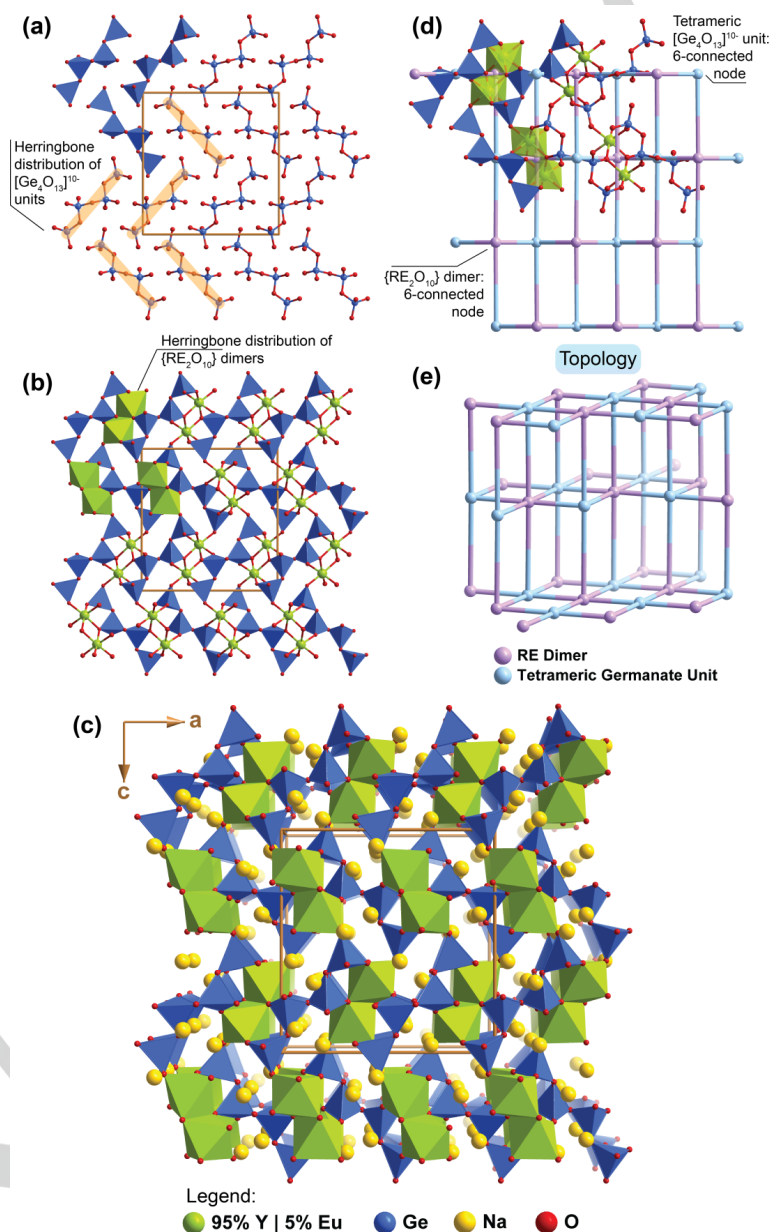


Figure 3. (a) Herringbone distribution of anionic tetrameric $[\text{Ge}_4\text{O}_{13}]^{10-}$ units in the ac plane of the unit cell. (b) Anionic $[\text{RE}_2\text{Ge}_4\text{O}_{13}]_n^{4n-}$ network formed by connection between adjacent tetramers via $\{\text{Ge}_2\text{O}_{10}\}$ dimers. (c) Mixed polyhedral and ball-and-stick representation of the crystal packing of $\text{Na}_4[(\text{Y}_{0.95}\text{Eu}_{0.05})_2\text{Ge}_4\text{O}_{13}]$ (**1**) viewed along the $[010]$ direction of the unit cell. Topological analysis of the inorganic framework: (d) identification of the anionic tetrameric $[\text{Ge}_4\text{O}_{13}]^{10-}$ units and $\{\text{Ge}_2\text{O}_{10}\}$ dimers as 6-connected nodes; (e) uninodal 6-connected network with the **pcu** α -Po primitive cubic topological type.

Photoluminescence Properties

Trivalent lanthanide ions present exceptional luminescence properties, ranging from the UV-Visible to the near infrared regions,^[17] and find major technological applications in lasers, telecommunications, displays, lighting, pressure sensors, security inks and marking, barcoding, luminescent thermometry, bioimaging and immunoassays.^[18] Here, photoluminescent materials were obtained by replacing 10% of optically silent Y^{3+} , used as a diluting element, by Eu^{3+} and Tb^{3+} for visible emission, and Yb^{3+} and Er^{3+} for near infrared emission. Additionally, the up-conversion emission is achieved with a sample containing only Yb^{3+} and Er^{3+} . We have prepared $Na_4[(Y_{0.9}Eu_{0.1})_2Ge_4O_{13}]$ (**2**), $Na_4[(Y_{0.9}Tb_{0.1})_2Ge_4O_{13}]$ (**3**), $Na_4[(Y_{0.90}Yb_{0.09}Er_{0.01})_2Ge_4O_{13}]$ (**4**) and $Na_4[(Yb_{0.9}Er_{0.1})_2Ge_4O_{13}]$ (**5**) (Experimental Section). The experimental powder X-ray diffraction patterns of these samples are identical and in accord with the powder pattern simulated from the single-crystal X-ray structure (Figure 4). As shown for **2** (Figure S2 in SI), these materials are thermally stable up to 1273 K. At 1373 K the crystal structure begins decomposing, resulting in the crystallization of some $Na_{3.70}Ca_{1.15}Ge_3O_9$ (ICDD no. 04-009-4326), where Ca^{2+} is replaced by RE^{3+} ions with a decrease of the Na^+ charge balancing cations, affording $Na_{2.55}(Y, Eu)_{1.15}Ge_3O_9$. At 1473 K, the as-synthesized material is totally transformed into a mixture of the latter phase and $NaY(GeO_4)$ (ICDD no. 04-008-8315; Figure S2).

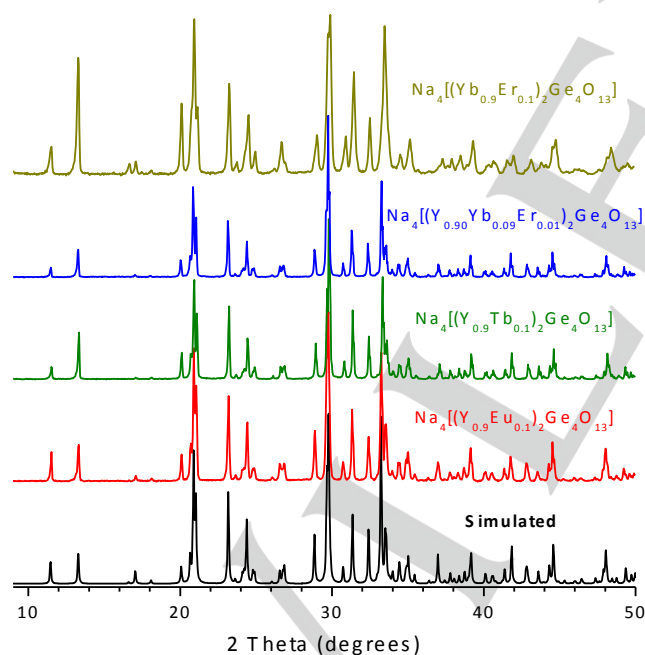


Figure 4. Experimental and simulated powder X-ray diffraction patterns of $Na_4[(Y_{0.9}Eu_{0.1})_2Ge_4O_{13}]$, $Na_4[(Y_{0.9}Tb_{0.1})_2Ge_4O_{13}]$, $Na_4[(Y_{0.90}Yb_{0.09}Er_{0.01})_2Ge_4O_{13}]$ and $Na_4[(Yb_{0.9}Er_{0.1})_2Ge_4O_{13}]$.

The excitation spectra of $Na_4[(Y_{1.8}Eu_{0.2})Ge_4O_{13}]$ and $Na_4[(Y_{1.8}Tb_{0.2})Ge_4O_{13}]$ were recorded at room temperature (ca.

300 K) and 12 K monitoring the strongest $Eu^{3+} {}^5D_0 \rightarrow {}^7F_2$, and the $Tb^{3+} {}^5D_4 \rightarrow {}^7F_5$ emission transitions (Figure 5). A broad UV band dominates the spectra, ranging from 230 to 275 nm and from 235 to 300 nm for Eu^{3+} and Tb^{3+} excitations, respectively. These bands are attributed to the inter-configurational spin-forbidden $4f^8 \rightarrow 4f^7 5d^1$ transition of Tb^{3+} , and to spin-allowed $4f^6 \rightarrow 4f^5 5d^1$ transition of Eu^{3+} because their energies are very similar to the energy reported for layered Eu^{3+} and Tb^{3+} silicates.^[2a] The additional sharp lines in the spectra of **2** and **3** are ascribed to the intra- $4f^6$ ${}^7F_{0,1} \rightarrow {}^5D_{1-4}$, 5L_6 , ${}^5G_{2-6}$, ${}^5H_{3-7}$ and ${}^5F_{1-5}$ transitions of Eu^{3+} , and to the intra- $4f^8$ ${}^7F_6 \rightarrow {}^5D_{2-4}$, 5G_J and 5H_7 transitions of Tb^{3+} .

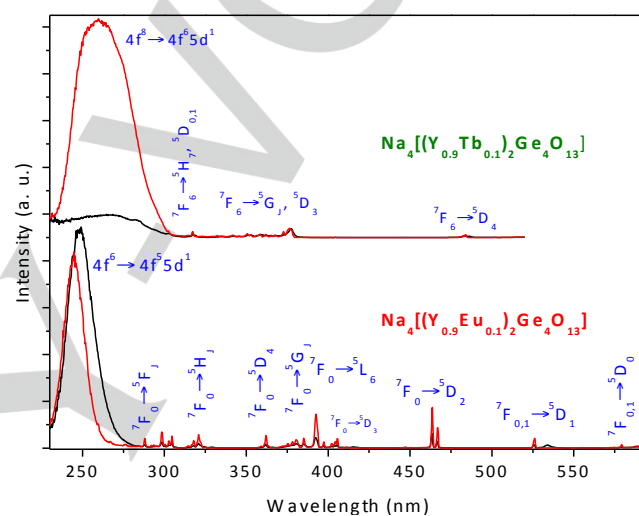


Figure 5. Excitation spectra of $Na_4[(Y_{0.9}Eu_{0.1})_2Ge_4O_{13}]$ ($\lambda_{em} = 610$ nm) and $Na_4[(Y_{0.9}Tb_{0.1})_2Ge_4O_{13}]$ ($\lambda_{em} = 551$ nm) recorded at room temperature (black lines) and 12 K (red lines).

The emission spectra of **2** and **3** recorded at room temperature and 12 K, excited at 392.5 and 377 nm, respectively, are shown in Figure 6. The sharp Eu^{3+} and Tb^{3+} emission lines are assigned to the ${}^5D_0 \rightarrow {}^7F_{0-4}$ and ${}^5D_4 \rightarrow {}^7F_{6-0}$ transitions, respectively. The emission spectra of **2** show a dominance of the ${}^5D_0 \rightarrow {}^7F_2$ over the ${}^5D_0 \rightarrow {}^7F_1$ transition. Even at room temperature, the Eu^{3+} emission spectrum exhibits for the ${}^5D_0 \rightarrow {}^7F_1$ and ${}^5D_0 \rightarrow {}^7F_2$ transitions a minimum of five and six Stark components, respectively, in accord with the presence of at least two low-symmetry Eu^{3+} environments in the crystal structure. In addition, the 12 K emission spectra excited at 392.5 and 250 nm (inset in Figure 6), bears evidence to two distinct sets of three Stark components in the ${}^5D_0 \rightarrow {}^7F_1$ region, and the presence of two very close ${}^5D_0 \rightarrow {}^7F_0$ transitions. These features are in perfect agreement with crystal structure, which calls for the presence of two distorted octahedral RE^{3+} centers in a dimeric unity. The assignment of the Eu^{3+} emission features of each site may be accomplished using the relationship between the covalency of the local Eu^{3+} environments, the nephelauxetic effect (affecting the energy of the ${}^5D_0 \rightarrow {}^7F_0$ transition),^[19] and the energy difference between the outer 7F_1 Stark components, $\Delta E({}^7F_1)$.^[20]

In accordance, site II is more covalent than site I because it presents lower ${}^5D_0 \rightarrow {}^7F_0$ transition energy, and lower $\Delta E({}^7F_1)$ (inset of Figure 6). However, the similarity of the two RE³⁺ crystallographic sites does not allow an unambiguous assignment. Although with a residual contribution, at 12 K the ${}^5D_1 \rightarrow {}^7F_{0,4}$ emission transitions of Eu³⁺ are observed (Figure S3 in the SI). We have measured the 5D_0 and 5D_4 lifetimes of Eu³⁺ and Tb³⁺ materials using intra-4f excitation at 392.5 (5L_6 level of Eu³⁺) and 376 nm (5D_3 level of Tb³⁺), respectively. At 12 K, it was possible to measure the 5D_0 lifetime of the two individual Eu³⁺ sites by selective detection at 589.2 nm (site I: 3.61±0.01 ms) and 590.6 nm (site II: 3.06±0.01 ms) (Figure S4a in the SI). However, at room temperature selective detection was not possible as the decay curves monitored at 589.2 and 590.6 nm are identical (and essentially mono-exponentials). An average 5D_0 lifetime of 3.01±0.01 ms was determined by measuring the decay curve at 610 nm (emission maximum). For Tb³⁺, selective detection of the two sites was not possible at both room temperature and 12 K. Monitoring at 551 nm (emission maximum), lifetimes of 3.38±0.02 ms (room temperature) and 3.70±0.02 ms (12 K) were obtained (Figure S4b in the SI). These data, point out the similarity of the lifetimes of the two RE³⁺ coordination sites.

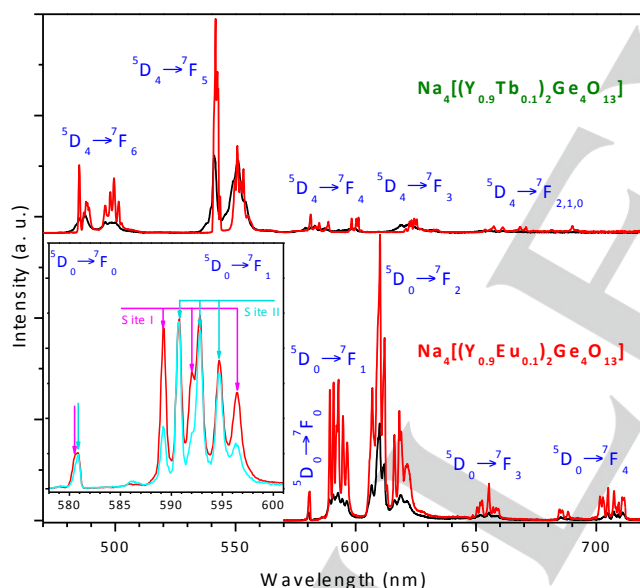


Figure 6. Emission spectra of $\text{Na}_4[(\text{Y}_{0.9}\text{Eu}_{0.1})_2\text{Ge}_4\text{O}_{13}]$ ($\lambda_{\text{exc.}} = 392.5$ nm) and $\text{Na}_4[(\text{Y}_{0.9}\text{Tb}_{0.1})_2\text{Ge}_4\text{O}_{13}]$ ($\lambda_{\text{exc.}} = 376$ nm) recorded at room temperature (black lines) and 12 K (red lines). The inset shows the $\text{Eu}^{3+} {}^5D_1 \rightarrow {}^7F_{0,1}$ transitions region recorded at 12 K using excitation wavelengths of 376 (red line) and 250 nm (cyan line).

Room temperature absolute emission quantum yields were measured for the red (**2**) and green (**3**) emitters. For **2**, the values measured for 254 nm and 393 nm excitation were 0.42±0.04 and 0.26±0.03, respectively, while for **3** the values measured at 254 nm and 377 nm excitation were 0.020±0.002 and 0.22±0.02, respectively.

The excitation spectra of $\text{Na}_4[(\text{Y}_{1.8}\text{Yb}_{0.18}\text{Er}_{0.02})\text{Ge}_4\text{O}_{13}]$ detecting the Er³⁺ and the Yb³⁺ near infrared emissions at room temperature and 12 K are shown in Figure 7. The spectra present a broad charge transfer UV band from 250 to 350 nm. According to Van Pieterse *et al.*, the associated charge-transfer process comprises the transfer of an electron from the ligand to the Yb³⁺, with reorganization of the charge density distribution on the metal ion.^[21] Under excitation in the charge-transfer absorption band the 4f levels of Yb³⁺ are populated via non-radiative relaxation. The Er³⁺ excitation spectra also show prominent sharp lines, ascribed to intra-4f¹¹ Er³⁺ transitions between the ${}^4I_{15/2}$ and the ${}^4F_{9/2,7/2,5/2,3/2}$, ${}^4S_{3/2}$, ${}^2H_{11/2,9/2}$, ${}^4G_{11/2}$, and ${}^2K_{15/2}$ levels. Both at room temperature and 12 K, Er³⁺ excitation is more efficient via the Yb³⁺-to-Er³⁺ energy transfer process since the Yb³⁺ ${}^2F_{7/2} \rightarrow {}^2F_{5/2}$ transition (from 875 to 1000 nm) dominates the spectra. On the other hand, at room temperature, Er³⁺-to-Yb³⁺ energy transfer also occurs, as witnessed by the Er³⁺ ${}^2K_{15/2}$, ${}^4G_{11/2}$ and ${}^2H_{11/2}$ levels in the Yb³⁺ excitation spectrum. Thus, both Yb³⁺-to-Er³⁺ and Er³⁺-to-Yb³⁺ energy transfer processes occur (inset in Figure 7). However, in contrast with the Yb³⁺-to-Er³⁺ energy transfer, which arises between two resonant excited levels (${}^2F_{5/2}$ of Yb³⁺ and ${}^4I_{9/2}$ of Er³⁺), the energy gap between the Er³⁺ donor level (${}^4F_{9/2}$) and the Yb³⁺ emitting level (${}^2F_{5/2}$), ca. 2800 cm⁻¹, is too large for an efficient energy transfer process to take place.

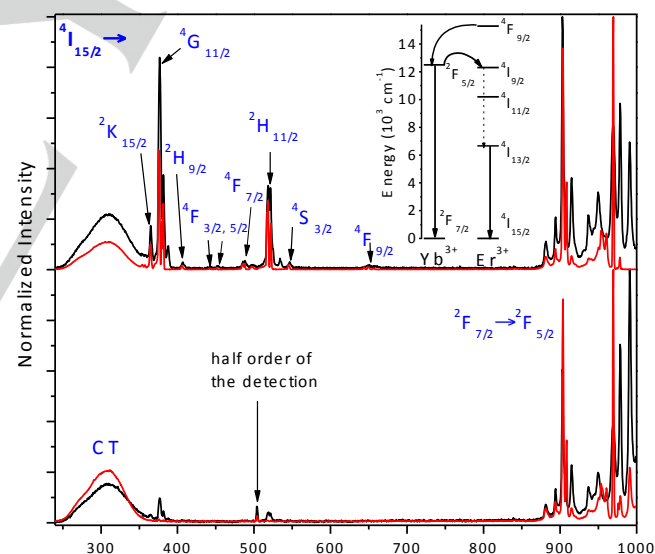


Figure 7. Excitation spectra of $\text{Na}_4[(\text{Y}_{0.90}\text{Yb}_{0.09}\text{Er}_{0.01})_2\text{Ge}_4\text{O}_{13}]$ with the detection fixed at 1010 nm (Yb³⁺ emission; bottom) and at 1540.5 nm (Er³⁺ emission; top) recorded at room temperature (black lines) and 12 K (red lines). The inset shows a simplified energy diagram of Yb³⁺ and Er³⁺ with the possible mechanism for the room-temperature energy transfer processes.

Figure 8 shows the near infrared emission spectra of **4** (excited at 903 nm; ${}^2F_{5/2}$ level of Yb³⁺) recorded at room temperature and 12 K. The emission lines are assigned to the ${}^2F_{5/2} \rightarrow {}^2F_{7/2}$ emission transition of Yb³⁺ and to the ${}^4I_{13/2} \rightarrow {}^4I_{15/2}$ transition of Er³⁺. The 12 K emission spectrum displays ${}^4I_{13/2} \rightarrow {}^4I_{15/2}$ local-field

structure with, at least, 10 Stark components, again supporting the presence of two distinct optically active Er^{3+} sites, in accord with the crystal structure. Upon raising the temperature from 12 K to room temperature, both emissions decrease significantly: whereas the integrated intensity of the Yb^{3+} transition decreases four fold, the Er^{3+} transition decreases only 1.5 times. This distinct temperature dependence of the two transitions is due to the progressive thermal intensification of the Yb^{3+} -to- Er^{3+} energy transfer process.

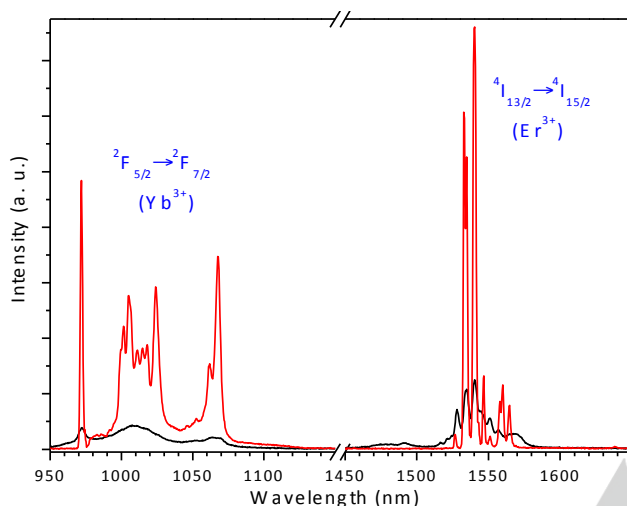


Figure 8. Emission spectra of $\text{Na}_4[(\text{Y}_{0.90}\text{Yb}_{0.09}\text{Er}_{0.01})_2\text{Ge}_4\text{O}_{13}]$ ($\lambda_{\text{exc.}} = 903 \text{ nm}$) recorded at room-temperature (black line) and 12 K (red line).

A preliminary luminescence study of **5** demonstrates that the $\text{Na}_4[\text{RE}_2\text{Ge}_4\text{O}_{13}]$ system features up-conversion emission, a property seldom reported for rare-earth crystalline germanates. Upon 980 nm excitation, $\text{Na}_4[(\text{Yb}_{0.9}\text{Er}_{0.1})_2\text{Ge}_4\text{O}_{13}]$ emits red light attributed to $\text{Er}^{3+} {}^4\text{F}_{9/2} \rightarrow {}^4\text{I}_{15/2}$ emission transition (Figure 9a). The green emissions, ${}^2\text{H}_{11/2} \rightarrow {}^4\text{I}_{15/2}$ and ${}^4\text{S}_{3/2} \rightarrow {}^4\text{I}_{15/2}$, are also observed with much lower intensity. These three visible Er^{3+} emissions present a distinct dependence on the excitation power, as shown by double-log plots of the up-conversion emission versus power density and determined slopes (Figure 9b).

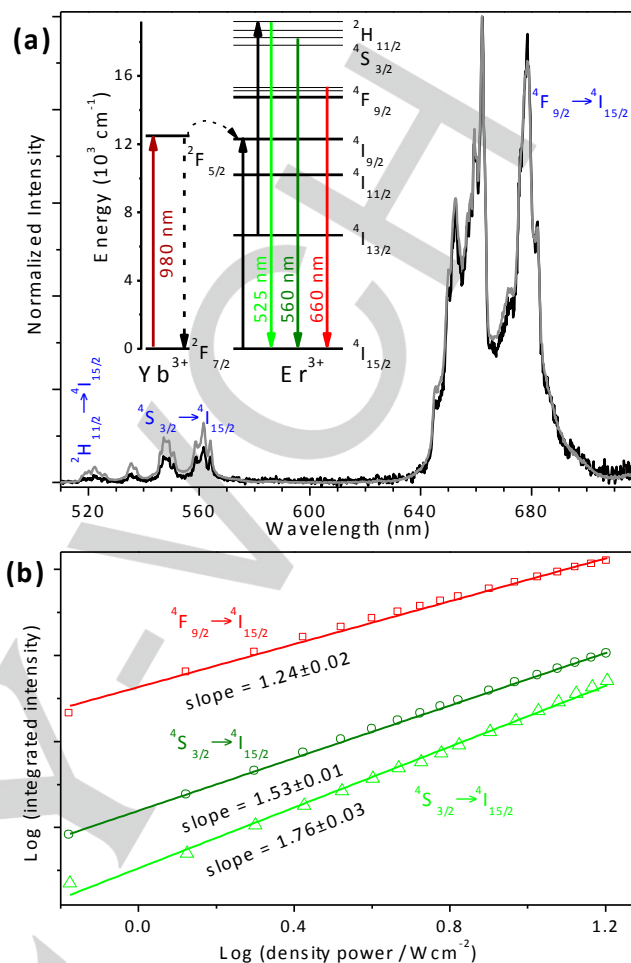


Figure 9. (a) Normalized up-conversion emission spectra of $\text{Na}_4[(\text{Yb}_{0.9}\text{Er}_{0.1})_2\text{Ge}_4\text{O}_{13}]$ recorded using a power density excitation of 1.33 Wcm^{-2} (black line) and 6.67 Wcm^{-2} (grey line) from a 980 nm continuous wave laser diode. The inset depicts $\text{Yb}^{3+}/\text{Er}^{3+}$ partial energy level diagrams showing the most likely Yb^{3+} -to- Er^{3+} energy transfer pathway. (b) Corresponding double-log plot of the Er^{3+} red and green up-conversion emission bands versus power density.

Conclusions

A new rare-earth germanate system, $\text{Na}_4[(\text{Y}_{1-a}\text{Ln}_a)_2\text{Ge}_4\text{O}_{13}]$ ($\text{Ln} = \text{Eu}, \text{Tb}$ or Yb and Er ; $a = 0.05, 0.1$), exhibiting visible and near infrared emission was synthesized. These materials crystallize in an orthorhombic non-centrosymmetric $\text{Pna}2_1$ structure, thermally stable up to 1273 K. The very dense framework is built up of unprecedented anionic tetrameric $[\text{Ge}_4\text{O}_{13}]^{10-}$ units, tetrameric units of $\{\text{GeO}_4\}$ tetrahedra, and isolated dimeric units encompassing two distinct distorted $\{\text{REO}_6\}$ octahedral. The Eu^{3+} photoluminescence, in particular at 12 K, confirmed the presence of two very similar RE^{3+} local sites. However, the crystallographic similarities of these two sites do not allow an unequivocal assignment of the individual transition lines and lifetimes to each of the observed Eu^{3+} sites. Incorporation of

Yb^{3+} and Er^{3+} shows that this rare-earth germanate system is also suitable for up-conversion emission.

Experimental Section

Synthesis. Rare-earth germanates were synthesized under static hydrothermal conditions using Teflon-lined autoclaves, in ovens preheated at 503 K. Rare-earth nitrate aqueous solutions ($0.4 \text{ mol}\cdot\text{dm}^{-3}$) were prepared by dissolving the corresponding oxides (99.99% purity in rare-earth oxide, Jinan Henghua Sci. & Tec. Co. Ltd.) with stoichiometric amounts of diluted nitric acid under heating.

Typical synthesis of $\text{Na}_4[(\text{Y}_{0.95}\text{Eu}_{0.05})_2\text{Ge}_4\text{O}_{13}]$ single-crystal sample (best crystals for X-ray analysis). An alkaline solution was made by dissolving 1.80 g GeO_2 (99.99%, Jinan Henghua Sci. & Tec. Co. Ltd.) with 9.00 g H_2O and 3.13 g NaOH (99%, AnalaR Normapur®). A mixture of 0.50 ml $\text{Eu}(\text{NO}_3)_3$ $0.4 \text{ mol}\cdot\text{dm}^{-3}$ and 4.50 ml $\text{Y}(\text{NO}_3)_3$ $0.4 \text{ mol}\cdot\text{dm}^{-3}$ aqueous solutions was added to this solution and stirred thoroughly. The gel, with composition 2.27 Na_2O : 1.00 GeO_2 : 0.052 Y_2O_3 : 0.0058 Eu_2O_3 : 29.06 H_2O , was reacted in Teflon lined autoclaves (volume 21 cm^3) for 6 days at 503 K. After synthesis, the autoclaves were removed from the oven and quenched in cold water. The final product consisted of single-crystals and very small particles of an unknown impurity, which were discarded. The single-crystals were separated by precipitation in five cycles using distilled water. The final sample was dried at 353 K overnight. $\text{Na}_4[(\text{Y}_{0.9}\text{Eu}_{0.1})_2\text{Ge}_4\text{O}_{13}]$, $\text{Na}_4[(\text{Y}_{0.9}\text{Tb}_{0.1})_2\text{Ge}_4\text{O}_{13}]$, $\text{Na}_4[(\text{Y}_{0.90}\text{Yb}_{0.09}\text{Er}_{0.01})_2\text{Ge}_4\text{O}_{13}]$ and $\text{Na}_4[(\text{Yb}_{0.9}\text{Er}_{0.1})_2\text{Ge}_4\text{O}_{13}]$ samples were synthesized in a similar way, by adjusting the Ln^{3+} amounts (from $0.4 \text{ mol}\cdot\text{dm}^{-3}$ nitrate solutions) to the desired concentration in the initial gel, but ca. 5 mg of pure sample (obtained, as mentioned above, by five-cycles precipitation) was added to the initial gel as seeds to ensure the achievement of the pure phase samples. These samples were collected as pure phases only by simple filtration. The syntheses give close to 100% yields in terms of the Ln^{3+} inserted in the parent gel, thus the relative concentration of lanthanides. The rare-earth compositions of the samples were ascertained by EDS, which did not show significant deviations from the nominal synthesis composition, and also showing a homogeneous distribution of Ln^{3+} and Y^{3+} ions over the crystals. The morphology of all samples was ascertained by SEM (Figure S5 in the SI).

Single-Crystal X-ray Diffraction Studies. Small single crystals of compound $\text{Na}_4[(\text{Y}_{0.95}\text{Eu}_{0.05})_2\text{Ge}_4\text{O}_{13}]$ (**1**) were directly harvested from the reaction vessel and immersed in highly viscous FOMBLIN Y perfluoropolyether vacuum oil (LVAC 140/13) purchased from Sigma-Aldrich. After careful inspection and selection, a suitable single-crystal of the material was mounted on Hampton Research CryoLoops^[22] with the help of a Stemi 2000 stereomicroscope equipped with Carl Zeiss lenses. Data were collected at 150(2) K on a Bruker X8 Kappa APEX II charge-coupled device (CCD) area-detector diffractometer (Mo K α graphite-monochromated radiation, $\lambda = 0.71073 \text{ \AA}$) controlled by the APEX2 software package^[23], and equipped with an Oxford Cryosystems Series 700 cryostream monitored remotely using the software interface Cryopad.^[24] Images were processed using the software package SAINT+,^[25] and data was corrected for absorption by the multi-scan semi-empirical method implemented in SADABS.^[26] The crystal structure was solved using the Patterson synthesis algorithm implemented in SHELXS-97^[27], which allowed the immediate location of most of the atoms in the asymmetric unit, in particular the rare-earth (RE^{3+}) centers and the tetrahedral Ge^{4+} sites. All remaining non-hydrogen atoms were located from difference Fourier maps calculated from successive full-matrix least squares refinement cycles on F^2 using 2017 SHELXL release.^[27a, 28] All non-hydrogen atoms were successfully refined using

anisotropic displacement parameters. All structural refinements were performed using the graphical interface ShelXle.^[29] The structure was found to be disordered concerning the occupancy of the heavy sites: the two crystallographically independent RE^{3+} sites may be occupied by both Y^{3+} and Eu^{3+} ; the site occupancy was found from unrestrained refinement with complementary rates of occupancy for each $\text{Y}^{3+}/\text{Eu}^{3+}$ pair; upon full least-squares convergence the respective site occupancy was fixed to give the molecular formulae quoted for each material. During the refinement stage, crystals of **1** yielded crystallographic evidence of being *twinning by inversion*. During the last stages of the least-squares refinement, the twin law (-1 0 0, 0 -1 0, 0 0 -1) (inversion operator) was considered along with one *BASF* parameter (equivalent to the Flack parameter^[30]), which refined to the value in Table 1. The last difference Fourier map synthesis showed the highest peak ($0.578 \text{ e}\text{\AA}^{-3}$) and deepest hole ($-0.737 \text{ e}\text{\AA}^{-3}$) at 0.99 \AA and 0.74 \AA from Ge3 and the mixed site Y1/Eu1, respectively. Structural drawings were created with the software package Crystal Impact Diamond.^[31] Information concerning crystallographic data collection and structure refinement details is summarized in Table 1. Detailed tabulated data on bond lengths and angles for the octahedral (RE^{3+}) and tetrahedral (Ge^{4+}) environments are given in Tables 2 to 4. Crystallographic information (excluding structure factors) may be obtained free of charge from Fachinformationszentrum Karlsruhe, 76344, Eggenstein-Leopoldshafen, Germany (e-mail: crysdata@fiz-karlsruhe.de), on quoting the depository numbers CSD-434102.

General Instrumentation. The crystal phase and purity of the samples were established by powder X-ray diffraction data collected at ambient temperature on a Emyrean PANalytical diffractometer ($\text{CuK}\alpha_{1,2}$ X-radiation, $\lambda_1=1.540598 \text{ \AA}$, $\lambda_2=1.544426 \text{ \AA}$) equipped with a fast PIXcel 1D detector and a flat-plate sample holder in a Bragg-Brentano parafocusing optics configuration (45 kV, 40 mA). Intensity data were collected by the step-counting method (step 0.04°), in continuous mode, in the $5 \leq 2\theta \leq 50^\circ$ range. SEM (Scanning Electron Microscopy) images were collected either with either a Hitachi S4100 or a high-resolution Hitachi SU-70, both working at 15 kV. EDS (Energy Dispersive X-Ray Spectroscopy) data was recorded using the latter microscopes coupled with a Bruker Quantax 400 or a Sprit 1.9 EDS microanalysis system.

Photoluminescence. The emission and excitation spectra were recorded on a Fluorolog-2[®] Horiba Scientific (Model FL3-2T) spectroscope, with a modular double grating excitation spectrometer (fitted with a 1200 grooves/mm grating blazed at 330 nm) and a TRIAX 320 single emission monochromator (fitted with a 1200 grooves/mm grating blazed at 500 nm, reciprocal linear density of $2.6 \text{ nm}\cdot\text{mm}^{-1}$), coupled to a R928 (visible detection) or a H9170 (near infrared detection) Hamamatsu photomultiplier, using the front face acquisition mode. The excitation source was a 450 W Xe arc lamp. The emission spectra were corrected for detection and optical spectral response of the spectrofluorometer and the excitation spectra were corrected for the spectral distribution of the lamp intensity using a photodiode reference detector. Time-resolved measurements were carried out on a 1934D3 phosphorimeter coupled to the Fluorolog-3, and a Xe-Hg flash lamp (6 μs /pulse half width and 20-30 μs tail) was used as the excitation source. The low-temperature measurements were performed using a helium-closed cycle cryostat with vacuum system measuring ca. 10^{-6} mbar and a Lakeshore 330 auto-tuning temperature controller with a resistance heater. For the up-conversion measurements, a 980 nm continuous wave laser diode (CrystaLaser, DL980-3W0-TO) was used as the excitation source, with the laser beam area of 0.15 cm^2 , according to the manufacturer. The laser power was tunable up to a maximum output power of 3 W.

The absolute emission quantum yields were measured at room temperature using a quantum yield measurement system C9920-02 from Hamamatsu with a 150 W Xenon lamp coupled to a monochromator for wavelength discrimination, an integrating sphere as sample chamber and a multi-channel analyser for signal detection. Three measurements were made for each sample so that the average value is reported. The method is accurate to within 10 %.

Acknowledgements

We would like to thank Fundação para a Ciência e a Tecnologia (FCT, Portugal) for funding. This work was developed in the scope of the project CICECO – Aveiro Institute of Materials POCI-01-0145-FEDER-007679 (Ref. FCT UID/CTM/50011/2013), financed by national funds through the FCT/MEC and when applicable co-financed by FEDER under the PT2020 Partnership Agreement. D.A. thanks FCT for a postdoctoral grant (SFRH/BPD/95032/2013).

Keywords: Germanates; Rare-Earths; Lanthanides; Photoluminescence; Up-conversion

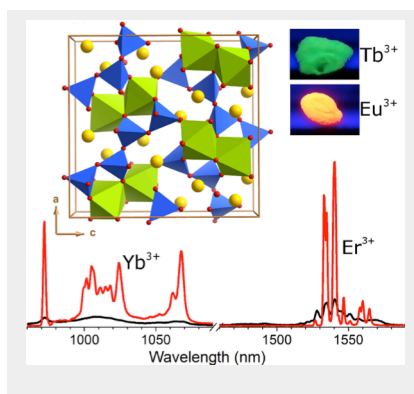
- [1] a) D. Ananias, M. Kostova, M.; F. A. A. Paz, A. N. C. Neto, R. T. De Moura, O. L. Malta, L. D. Carlos, J. Rocha, *J. Am. Chem. Soc.* **2009**, *131*, 8620–8626; b) D. Ananias, F. A. A. Paz, L. D. Carlos, C. F. G. C. Geraldes, J. Rocha, *Angew. Chem., Int. Ed.* **2006**, *45*, 7938–7942; c) D. Ananias, J. P. Rainho, A. Ferreira, J. Rocha, L. D. Carlos, *J. Alloys Compd.* **2004**, *374*, 219–222; d) A. Ferreira, D. Ananias, L. D. Carlos, C. M. Morais, J. Rocha, *J. Am. Chem. Soc.* **2003**, *125*, 14573–14579.
- [2] a) D. Ananias, M. Kostova, F. A. A. Paz, A. Ferreira, L. D.; Carlos, J. Klinowski, J. Rocha, *J. Am. Chem. Soc.* **2004**, *126*, 10410–10417; b) D. Ananias, S. Ferdov, F. A. A. Paz, R. A. Sá Ferreira, A. Ferreira, C. F. G. C. Geraldes, L. D. Carlos, Z. Lin, J. Rocha, *Chem. Mater.* **2008**, *20*, 205–212.
- [3] a) D. Ananias, A. Ferreira, L. D. Carlos, J. Rocha, *Adv. Mater.* **2003**, *12*, 980–985; b) D. Ananias, L. D. Carlos, J. Rocha, *Opt. Mater.* **2006**, *28*, 582–586; c) D. Ananias, F. A. A. Paz, D. S. Yufit, L. D. Carlos, J. Rocha, *J. Am. Chem. Soc.* **2015**, *137*, 3051–3058.
- [4] D. Ananias, F. A. A. Paz, L. D. Carlos, J. Rocha, *Microporous Mesoporous Mat.* **2013**, *166*, 50–58.
- [5] P. L. Chen, P. Y. Chiang, H. C. Yeh, B. C. Chang, K. H. Lii, *Dalton Trans.* **2008**, 1721–1726.
- [6] X. Zhao, K. Wang, T. Yan, Y. Yan, B. Zou, J. Yu, R. Xu, *Chin. J. Chem.* **2012**, *30*, 2066–2072.
- [7] X. Zhao, T. Yan, K. Wang, Y. Yan, B. Zou, J. Yu, R. Xu, *Eur. J. Inorg. Chem.* **2012**, 2527–2532.
- [8] J. Yeon, J. B. Hardaway, A. S. Sefat, A. M. Latshaw, H. –C. zur Loye, *Solid State Sci.* **2014**, 3424–30.
- [9] X. Wang, Y. Wang, Q. Liu, Y. Li, J. Yu, R. Xu, *Inorg. Chem.* **2012**, *51*, 4779–4783.
- [10] W. Liu, M. Yang, Y. Ji, F. Liu, Y. Wang, X. Wang, X. Zhao, X. Liu, *RSC Adv.* **2014**, *4*, 26951–26955.
- [11] Y. A. Gorbunov, B. A. Maksimov, N. V. Belov, *Dokl. Akad. Nauk SSSR* **1973**, *211*, 591–594.
- [11] W. H. Baur, *Acta Cryst. B* **1974**, *30*, 1195–1215.
- [12] S. P. Liu, M. L. Chen, B. C. Chang, K. H. Lii, *Inorg. Chem.* **2013**, *52*, 3990–3994.
- [13] J. H. Zhang, P. X. Li, J. G. Mao, *Dalton Trans.* **2010**, 39, 5301–5305.
- [14] C. F. Macrae, I. J. Bruno, J. A. Chisholm, P. R. Edgington, P. McCabe, E. Pidcock, L. Rodriguez-Monge, R. Taylor, J. van de Streek, P. A. Wood, *J. Appl. Crystallogr.* **2008**, *41*, 466–470.
- [15] a) A. L. Spek, *J. Appl. Crystallogr.* **2003**, *36*, 7–13; b) A. L. Spek, *Acta Cryst. A* **1990**, *46*, C34.
- [16] V. A. Blatov, A. P. Shevchenko, D. M. Proserpio, *Cryst. Growth Des.* **2014**, *14*, 3576–3586.
- [17] J.-C. G. Bünzli and C. Piguet, *Chem. Soc. Rev.* **2005**, *34*, 1048–1077.
- [18] a) J.-C. G. Bünzli, *Eur. J. Inorg. Chem.* **2017**, 5058–5063; b) J. Rocha, C. D. S. Brites, L. D. Carlos, *Chem. Eur. J.* **2016**, *22*, 14782 – 14795; c) S. V. Eliseeva, J.-C. G. Bünzli, *Chem. Soc. Rev.* **2010**, *39*, 189–227.
- [19] L. D. Carlos, O. L. Malta, R. Q. Albuquerque, *Chem. Phys. Lett.* **2005**, *415*, 238–242.
- [20] W. T. Carnall, H. Crosswhite, H. M. Crosswhite, Energy Level Structure and Transition Probabilities of the TriValent Lanthanides in LaF₃; Argonne National Laboratory: Argonne, IL, **1977**.
- [21] L. van Pieterse, M. Heeroma, E. de Heer, A. Meijerink, *J. Lumin.* **2000**, *91*, 177–193.
- [22] T. Kottke, D. Stalke, *J. App. Cryst.* **1993**, *26*, 615–619.
- [23] APEX2, Data Collection Software Version 2.1-RC13, Bruker AXS, Delft, The Netherlands **2006**.
- [24] Cryopad, Remote monitoring and control, Version 1.451, Oxford Cryosystems, Oxford, United Kingdom **2006**.
- [25] SAINT+, Data Integration Engine v. 7.23a © 1997–2005, Bruker AXS, Madison, Wisconsin, USA.
- [26] G. M. Sheldrick, SADABS v.2.01, Bruker/Siemens Area Detector Absorption Correction Program **1998**, Bruker AXS, Madison, Wisconsin, USA.
- [27] a) G. M. Sheldrick, *Acta Cryst. A* **2008**, *64*, 112–122; b) G. M. Sheldrick, SHELXS-97, Program for Crystal Structure Solution, University of Göttingen **1997**.
- [28] a) G. M. Sheldrick, SHELXL - Crystal Structure Refinement, Version 2017/1, Program for Crystal Structure Refinement, University of Göttingen **1993–2017**; b) G. M. Sheldrick, *Acta Cryst. C* **2015**, *71*, 3–8.
- [29] C. B. Hübschle, G. M. Sheldrick, B. Dittrich, *J. Appl. Crystallogr.* **2011**, *44*, 1281–1284.
- [30] a) H. D. Flack, G. Bernardinelli, *J. Appl. Crystallogr.* **2000**, *33*, 1143–1148; b) H. D. Flack, G. Bernardinelli, *Acta Cryst. A* **1999**, *55*, 908–915; c) H. D. Flack, *Acta Cryst. A* **1983**, *39*, 876–881.
- [31] K. Brandenburg, DIAMOND, Version 3.2f. Crystal Impact GbR, Bonn, Germany **1997–2010**.

Entry for the Table of Contents (Please choose one layout)

Layout 1:

FULL PAPER

The framework of the new family of rare-earth germanates $\text{Na}_4(\text{Y}_{1-a}\text{Ln}_a)_2\text{Ge}_4\text{O}_{13}$ ($\text{Ln} = \text{Eu}, \text{Tb}$ or Yb and Er ; $a = 0.05, 0.1$) comprises unprecedented $[\text{Ge}_4\text{O}_{13}]^{10-}$ tetramers, among other units. These materials feature interesting photoluminescence properties in the visible and near-infrared spectral regions, while isomorphous $\text{Na}_4(\text{Yb}_{0.9}\text{Er}_{0.1})_2\text{Ge}_4\text{O}_{13}$ features up-conversion emission.



Rare-Earth Germanates*

Duarte Ananias,* Filipe A. Almeida Paz,
Luís D. Carlos and João Rocha*

Page No. – Page No.

Title

*one or two words that highlight the emphasis of the paper or the field of the study